Maximal Memory Capacity Near the Edge of Chaos in Balanced Cortical E-I Networks

Takashi Kanamaru
kanamaru@cc.kogakuin.ac.jp
International Research Center for Neurointelligence (WPI-IRCN), UTIAS,
University of Tokyo 113-0033, Japan, and Department of Mechanical Science
and Engineering, Kogakuin University, Tokyo 192-0015, Japan

Takao K. Hensch
hensch@ircn.jp
International Research Center for Neurointelligence (WPI-IRCN), UTIAS,
University of Tokyo 113-0033, Japan; Center for Brain Science, Harvard University,
Cambridge, MA 02138, U.S.A.; and FM Kirby Neurobiology Center,
Boston Children's Hospital, Boston, MA 02115, U.S.A.

Kazuyuki Aihara
kaihara@g.ecc.u-tokyo.ac.jp
International Research Center for Neurointelligence (WPI-IRCN), UTIAS,
University of Tokyo 113-0033, Japan

We examine the efficiency of information processing in a balanced excitatory and inhibitory (E-I) network during the developmental critical period, when network plasticity is heightened. A multimodule network composed of E-I neurons was defined, and its dynamics were examined by regulating the balance between their activities. When adjusting E-I activity, both transitive chaotic synchronization with a high Lyapunov dimension and conventional chaos with a low Lyapunov dimension were found. In between, the edge of high-dimensional chaos was observed. To quantify the efficiency of information processing, we applied a short-term memory task in reservoir computing to the dynamics of our network. We found that memory capacity was maximized when optimal E-I balance was realized, underscoring both its vital role and vulnerability during critical periods of brain development.

1 Introduction

It is known that neuronal circuits in the brain are particularly influenced by environmental inputs when their plasticity is elevated during critical periods (CPs) of development (Hensch, 2004, 2005; Werker & Hensch, 2015).

One of the best known examples is the loss of binocular vision following monocular deprivation of kittens (Hubel & Wiesel, 1970), which is not observed in adult cats. Similar CPs have been discovered in various systems across species, including sound localization in barn owls, song learning in birds, and speech perception in human infants (Hensch, 2004).

Late maturation of neuronal circuits utilizing the inhibitory neurotransmitter γ-amino butyric acid (GABA) dictates the opening of CPs (Hensch, 2005). In particular, the maturation of parvalbumin-positive (PV) basket cells, a subtype of inhibitory neuron, plays a pivotal role (Werker & Hensch, 2015; Reh et al., 2020). These PV cells extend lateral inhibition onto neighboring pyramidal cell bodies, which are excitatory neurons; therefore, the emergence of PV basket synapses realizes a balance between excitatory and inhibitory activity (E-I balance) at CP onset. Subsequent closure of the CP protects the circuits from further rewiring. Several factors actively promote stability, such as structural barriers like perineuronal nets or myelin-related signals, and the dampening of neuromodulatory systems (Werker & Hensch, 2015). Neuromodulatory systems, such as acetylcholine (ACh) and serotonin, act through another class of non-PV inhibitory interneuron, which ultimately form synaptic connections onto PV basket cells (Takesian et al., 2018). The emergence of molecules that dampen ACh receptors, like Lynx1, serve as a functional brake on plasticity. Removal of Lynx1 may restore a juvenile E-I balance to reopen CPs in adulthood (Morishita et al., 2010; Takesian et al., 2018).

Optimal E-I balance is thought to be homeostatically maintained in the brain to avoid runaway excitation or quiescence (Turrigiano & Nelson, 2004). Disrupted E-I balance commonly underlies developmental disorders such as autism or psychiatric disorders like schizophrenia (Eichler & Meier, 2008; Yizhar et al., 2011; Nelson & Valakh, 2015). In slices of ferret prefrontal or occipital cortex, the E-I balance generates self-sustaining activity that can be turned on and off by synaptic inputs (Shu, Hasenstaub, & McCormick, 2003). In the field of nonlinear dynamics, a theoretical model of a neural network with balanced E-I activity is known to yield deterministic chaos (van Vreeswijk & Sompolinsky, 1996). Other theoretical models composed of excitatory and inhibitory neurons show various synchronized dynamics, including a fully synchronized, stochastically synchronized, and chaotically synchronized (Brunel, 2000; Kanamaru & Sekine, 2005; Kanamaru & Aihara, 2008). Here, we examined the efficiency of information processing in a network with shifting E-I balance to understand the role of optimally balanced dynamics during the CP.

Specifically, we incorporated the framework of reservoir computing (Lukoševičius & Jaeger, 2009), wherein machine-learning tasks are solved using recurrent neural networks. During training, random connection weights inside the network are fixed, and only the weights in the output layer are trained. Some studies have found that networks show high performance when their parameters are set at the edge of chaos (Bertschinger

& Natschläger, 2004; Legenstein & Maass, 2007; Boedecker et al., 2012). In this study, we applied a short-term memory task to our network and considered the relationship between E-I balanced dynamics and CPs. In the short-term memory task, a quantity called memory capacity is calculated to evaluate how long information on time-varying inputs is retained in the network (Kubota et al., 2018; Tanaka et al., 2020).

In section 2 of this paper, we define a cortical network model composed of excitatory pyramidal neurons in layers 2/3 and inhibitory interneurons in layer 4. First, we define a module model composed of excitatory and inhibitory neurons and then define a multimodule network by connecting them to each other. In section 3, we examine dynamics of our model and find transitive chaotic synchronization and conventional chaos. In section 4, we analyze the chaotic dynamics in our model using the Lyapunov spectrum and Lyapunov dimensions. It was found that the Lyapunov dimension of transitive chaotic synchronization is high and that of conventional chaos is low. Between them, we also found a new type of the edge of chaos, the edge of high-dimensional chaos. In section 5, we quantify the degree of E-I balance using two E/I ratios: the functional E/I ratio proposed by Bruining et al. (2020) and the input E/I ratio, which is the proportion of excitatory to inhibitory input onto pyramidal neurons. Transitive chaotic synchronization and the edge of high-dimensional chaos were observed when both E/I ratios are close to 1. In section 6, we apply the short-term memory task in reservoir computing to the E-I balanced dynamics in our network. It was observed that memory capacity was maximized when optimal E-I balance was realized. Conclusions are discussed in the final section of this paper.

2 Model

2.1 Cortical Layers. To examine networks of excitatory and inhibitory neurons with shifting E-I balance, we considered ensembles of neurons in cortical layers as shown in Figure 1A (Kanamaru, Fujii, & Aihara, 2013). In particular, we constructed a network composed of excitatory pyramidal neurons (PYRs) in layers 2/3 and inhibitory interneurons (INs) in layer 4. We assumed that the interneurons in our model are parvalbumin-positive (PV), fast-spiking (FS) neurons because their maturation underlines an optimal E-I balance that opens the CP (Hensch, 2005; Reh et al., 2020). In Figure 1A, top-down glutamatergic and bottom-up pathways are shown as inputs to the network. When we examine the internal dynamics of the network, these inputs are omitted.

Notably, we also incorporated the effect of ascending projections from the nucleus basalis of Meynert (NBM) and their corticopetal acetylcholine (ACh) release when attention-demanding tasks are performed (Thiele & Bellgrove, 2018). In our model, ACh was projected onto INs bearing nicotinic acetylcholine receptors (nAChRs) in layer 1. These neurons in turn inhibit INs in layer 4 and, as a result, indirectly activate PYRs in layers 2/3
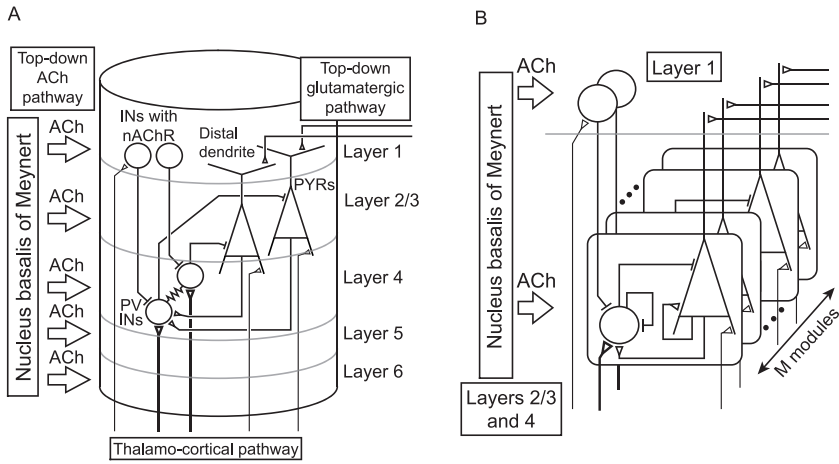
Figure 1: (A) Cortical layer structure. We consider a network composed of excitatory pyramidal neurons (PYRs) in layers 2/3 and inhibitory interneurons (INs) in layer 4 and layer 1 bearing nAChR. (B) M-module structure of a model.

(Takesian et al., 2018). Morishita et al. (2010) found that an endogenous prototoxin, Lynx1, suppresses nAChR signaling and closes the CP, potentially by modulating E-I circuit balance (Takesian et al., 2018).

This model is not a full model of the cortical circuitry because it does not incorporate inhibitory neurons in layers 2/3 or excitatory neurons in layer 4 for examples. Rather, it is a minimal model of cortical circuitry that is relevant to plasticity during CP (Werker & Hensch, 2015). This model allows us to focus on the particular E-I balance, which appears to be important for maximizing learning during CP in biological systems.

2.2 Module Model. We considered a multimodule network model of layers 2/3 and 4 of the cortex (see Figure 1B). Each module, shown as a rectangle with rounded corners, was composed of N_E excitatory neurons and N_I inhibitory neurons.

The internal states of the ith excitatory neuron and inhibitory neuron were described by phase variables $\theta_E^{(i)}$ and $\theta_I^{(i)}$, respectively (Kanamaru & Sekine, 2005; Kanamaru & Aihara, 2008). This phase model is often used as a model of class I spiking neurons (Hodgkin, 1948; Izhikevich, 1999, 2000). Arbitrary class I neurons near their bifurcation points can be transformed into this phase model. Even when neurons are not close to their bifurcation points, it is expected that similar results will be observed in both models. Chaotic dynamics observed in networks of phase models has also been observed in networks of the class I Morris-Lecar neuron model (Kanamaru, 2006, 2007). Moreover, this model can facilitate the analysis of its dynamics

in the limit of $N_E, N_I \to \infty$ by integrating its Fokker-Planck equations numerically, as shown below.

The activity of a single neuron in the model without connections can be regulated by inputs s_X ($X = E$ or I). When $s_X < 0$, a stable equilibrium point $\theta = \theta_0 \equiv \arccos((1 + s_X)/(1 - s_X))$ exists, which can be considered a resting state. When $s_X > 0$, the resting state disappears and θ starts to oscillate. Firing time is defined as the time at which $\theta_X^{(j)}$ exceeds π. In this study, we set $s_E, s_I < 0$. Each neuron without connections spontaneously fires owing to gaussian white noise $\xi_X^{(i)}(t)$ with strength D.

The connections among the neurons are global. We consider four types of intramodule connections: $E \to E$, $E \to I$, $I \to E$, and $I \to I$. Connections generating postsynaptic currents of an exponential form between all pairs of neurons, as well as diffusive connections by gap junctions between inhibitory neurons, are present. Appendix A provides a detailed definition of the module.

When there are no intramodule connections, all neurons show only stochastic firings owing to the gaussian white noise. Various collective firings were observed when intramodule connections were introduced. For weak E-I connections, only asynchronous firings with low or high firing rates are observed, depending on the strength D of the gaussian white noise. By adjusting the strengths of E-I connections, some correlations among the firings of different neurons appear, where ensemble-averaged firing rates of neurons show time-varying dynamics, such as periodic and chaotic dynamics (Kanamaru & Sekine, 2005; Kanamaru & Aihara, 2008). These dynamics are called intramodule synchronization.

The typical intramodule synchronization in a module with $N_E = 1000$ and $N_I = 250$ is shown in Figure 2A as a raster plot of the spikes of randomly selected 100 excitatory neurons and 25 inhibitory neurons. Methods for initializing models in Figure 2 are explained in appendix E. This synchronization is realized by intramodule connections. In Figure 2B, temporal changes in ensemble-averaged firing rates r_X ($X = E$ or I) defined as

$$r_X(t) \equiv \frac{1}{N_X d} \sum_{i=1}^{N_X} \sum_j \Theta(t - t_j^{(i)}), \tag{2.1}$$

$$\Theta(t) = \begin{cases} 1 & \text{for } 0 \leq t < d, \\ 0 & \text{otherwise,} \end{cases} \tag{2.2}$$

calculated from the simulation result in Figure 2A are shown. The width d of the time window was set as $d = 1.0$. r_E and r_I oscillate when the intramodule synchronization is observed. Note that the conventional ratio of 4:1 between N_E and N_I does not affect the dynamics of a module except for the amount of fluctuations because the interactions among neurons are scaled as $1/N_X$ ($X = E$ or I) as shown in equation A.3.
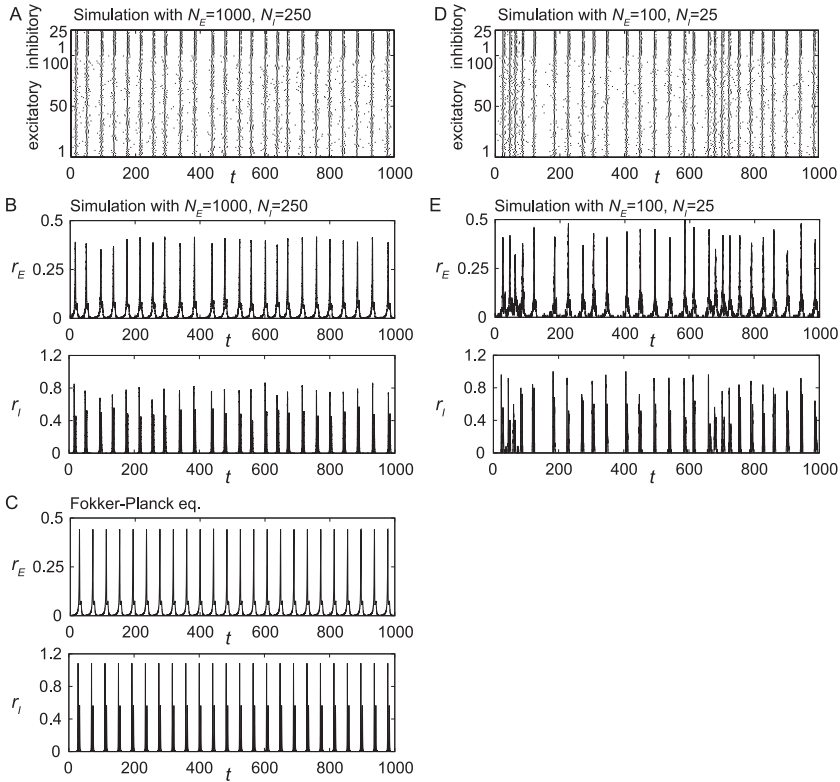
Figure 2: (A) Raster plot of the spikes of randomly selected 100 excitatory neurons and 25 inhibitory neurons in a module with $N_E = 1000$, $N_I = 250$, and $s_I = -0.03$. The values of the other parameters are shown in appendix A. Intramodule synchronization is observed. (B) Temporal changes in ensemble-averaged firing rates r_E and r_I defined by equation 2.1 that are calculated from the simulation in Figure 2A. r_E and r_I oscillate when the intramodule synchronization is observed. (C) Temporal changes in ensemble-averaged firing rates r_E and r_I of excitatory and inhibitory neurons, respectively, in a module with an infinite number of neurons obtained by analyzing the Fokker-Planck equations. The values of the parameters are the same with those used in Figure 2A. (D) Raster plot of the spikes of neurons in a smaller module with $N_E = 100$, $N_I = 25$, and $s_I = -0.03$. (E) Temporal changes in ensemble-averaged firing rates r_E and r_I calculated from the simulation in Figure 2D.

The averaged dynamics of a single module in the limit of $N_E, N_I \rightarrow \infty$ can be analyzed using the Fokker-Planck equations (FPEs), as shown in appendix B. By considering this limit, the equations that govern our model change from stochastic to deterministic, and we can calculate the

theoretical dynamics of ensemble-averaged firing rates r_E and r_I of excitatory and inhibitory neurons, respectively. Therefore, in the following sections, we examine the dynamics of our model in the limit of $N_E, N_I \to \infty$. When integrating the FPEs numerically, we transformed them into a set of ordinary differential equations (ODEs) using Fourier expansion as shown in appendix C. By replacing the original FPEs of a module with 242-dimensional ODEs, we can conduct nonlinear analysis of intramodule synchronization (Kanamaru & Sekine, 2005; Kanamaru & Aihara, 2008). To our knowledge, such simple analyses are possible only when the dynamics of the neurons is described by phase variables, as shown in appendix A.

Temporal changes in r_E and r_I calculated from the FPEs are shown in Figure 2C. They approximate well the ensemble-averaged firing rates in a module with a finite number of neurons shown in Figure 2B. In Figures 2A and 2B, the ratio of 4:1 between N_E and N_I did not affect the dynamics of a module except for the amount of fluctuations because of scaling of the connections of order $1/N_X$. Similarly, in the FPE-based analysis, the ratio between N_E and N_I disappears in the limit of $N_E, N_I \to \infty$.

The intramodule synchronization in a module with $N_E = 100$ and $N_I = 25$ is shown in Figures 2D and 2E. It is observed that the interpeak intervals of r_E and r_I are largely fluctuating in this small module. Comparison between Figure 2B and Figure 2E shows that the dynamics of a module with $N_E = 1000$ and $N_I = 250$ in Figure 2B better approximates the result of the FPE-based analysis shown in Figure 2C with smaller fluctuations.

This module is regarded as a model of a local E-I network, such as a pyramidal cell module (Rodriguez, Whitson, & Granger, 2004). Using these module models, we defined a network composed of M modules, as shown in Figure 1B. Previously, we had examined the pattern-retrieval dynamics of a multimodule network in which several patterns were embedded in the intermodule connections (Kanamaru, 2007; Kanamaru et al., 2013; Kanamaru & Aihara, 2019). Such networks can be interpreted as models of the adult brain, in which numerous memories are stored.

In contrast, in this study, we considered a model of the brain during development. Therefore, instead of embedding patterns in the intermodule connections, we randomly connected the modules. As intermodule connections, we treated two types of connections: those from excitatory neurons in the jth module to excitatory neurons in the ith module, and those from excitatory neurons in the jth module to inhibitory neurons in the ith module. Their strengths were defined as h_{ij}^{EE} and h_{ij}^{IE}, respectively, set to h^{EE} and h^{IE} with a probability of 0.1 and set to 0 with a probability of 0.9. The intermodule connections were also global.

A detailed definition of intermodule connections is provided in appendix D. In the following sections, we analyze the dynamics of a network with 48 such modules. Note that we can analyze this network using the FPEs of 48 modules, which are transformed into 48×242-dimensional ODEs.

3 Dynamics in a Network with Multiple Modules

In the following sections, we regulate E-I balance and observe the dynamics in a network with 48 modules. There are several methods for regulating E-I balance, such as regulating the ratio between N_E and N_I, regulating the activity of excitatory and inhibitory neurons, and regulating the strength of excitatory and inhibitory synapses. As stated in the previous section, the ratio between N_E and N_I does not affect the dynamics of our network except for the amount of fluctuations. Therefore, we use the other methods, that is, regulating the activity of neurons and regulating the strength of excitatory and inhibitory synapses.

In this section, we use parameter s_I to regulate the E-I balance, which controls the activity of inhibitory neurons. s_E and s_I can be interpreted as constant inputs to the excitatory and inhibitory neurons, respectively. Moreover, the regulation of s_I can be interpreted as the effect of input from layer 1 interneurons bearing nAChR, as shown in Figures 1A and 1B. In the following, s_I is the degree of inhibitory activity.

Dynamics of an E-I network with 48 modules for $s_I = -0.020$ are shown in Figure 3A. Methods for initializing this model in Figure 3 are explained in appendix E. Temporal changes in the ensemble-averaged firing rates r_{Ei} of the excitatory neurons in the ith module ($1 \leq i \leq 48$) were aligned such that they did not overlap. Figure 3B shows an enlarged image of Figure 3A. Temporal changes in a single r_{Ei} indicated that firing of the excitatory neurons in the ith module showed some correlations. This phenomenon shows intramodule synchronization. Some correlations were also observed among the ensemble-averaged firing rates of different modules, indicating intermodule synchronization that was also rearranged transitively.

The oscillation of the firing rate in each module was not periodic. In the next section, we show that the dynamics in Figure 3A are chaotic, that is, there are some positive Lyapunov exponents in the network. Therefore, we refer to the dynamics in Figure 3A as "transitive" chaotic synchronization.

The transitive chaotic synchronization observed with a different initial condition explained in appendix E is shown in Figure 3C. Even when starting from a different initial condition, the network converges to a similar transitive chaotic synchronization. Therefore, we assume that this dynamics is realized as some kind of attractor.

To elucidate the concept of transitive chaotic synchronization, we calculate the short covariance $\text{cov}_s(i, j)$ between r_{Ei} and r_{Ej} during a short period with $t' \leq t \leq t' + T$ written as

$$\text{cov}_s(i, j) = \frac{1}{T} \int_{t'}^{t'+T} (r_{Ei}(t) - \langle r_{Ei} \rangle)(r_{Ej}(t) - \langle r_{Ej} \rangle)\, dt, \tag{3.1}$$

where $\langle r_{Ei} \rangle$ and $\langle r_{Ej} \rangle$ are time averages of r_{Ei} and r_{Ej} during this period, respectively. Moreover, in order to consider the significance of $\text{cov}_s(i, j)$, we
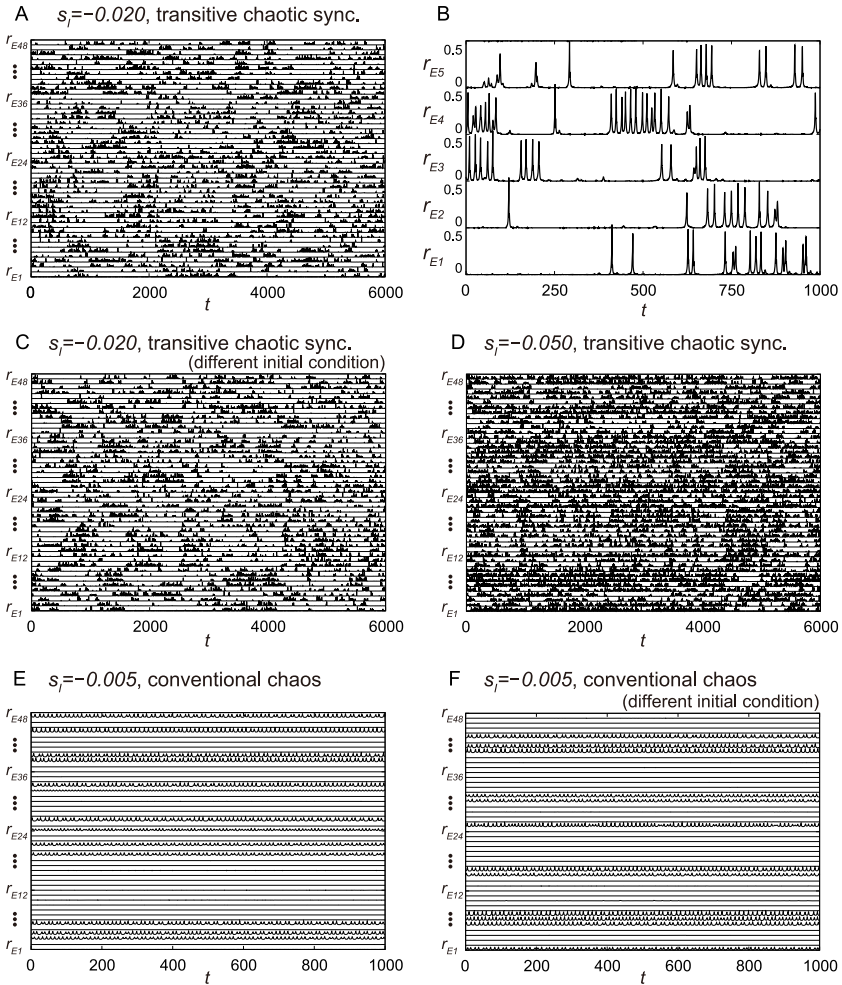
Figure 3: (A–C) Dynamics of a network with 48 modules for $s_I = -0.020$. (A) Temporal changes in the ensemble-averaged firing rates of excitatory neurons in a network with 48 modules are aligned so that they do not overlap. We can observe transitive chaotic synchronization in which modules showing intermodule synchronization are rearranged transitively. (B) An enlargement of Figure 3A. (C) Dynamics from a different initial condition (see appendix E). (D) Dynamics for $s_I = -0.050$. Due to E-I imbalance, the activity of excitatory neurons is dominant, and the firing rates of neurons are high. Transitive chaotic synchronization is still observed. (E–F) Dynamics for $s_I = -0.005$. (E) Due to the activity of inhibitory neurons becoming dominant, transitive chaotic synchronization disappears and conventional chaos emerges. (F) Dynamics from a different initial condition (see appendix E).
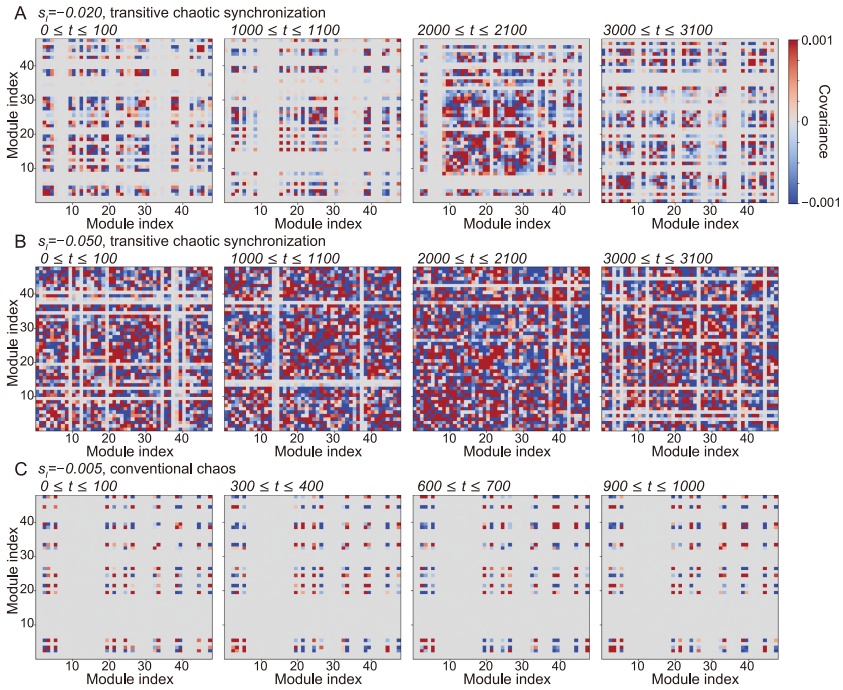
Figure 4: Color matrices of the short covariances $cov_s(i, j)$ between r_{Ei} and r_{Ej} during a short period for (A) $s_I = -0.020$, (B) $s_I = -0.050$, and (C) $s_I = -0.005$. When $cov_s(i, j)$ is inside the 99% confidence interval of the circular shuffles of $cov_s(i, j)$, it is replaced by 0. The red and blue dots show the in-phase and antiphase synchronization, respectively, between excitatory ensembles in the ith and jth modules. In Figures 4A and 4B, such synchronized pairs are rearranged when a different period is observed.

also calculate the circular shuffles (Madsen & Parra, 2022) of $cov_s(i, j)$ defined as

$$cov_s^{cs}(i, j) = \frac{1}{T} \int_{t'}^{t'+T} (r_{Ei}(t) - \langle r_{Ei} \rangle)(r_{Ej}(t + \tau) - \langle r_{Ej} \rangle) \, dt. \qquad (3.2)$$

The shift amount τ is chosen randomly 1000 times from a uniform distribution in (0, 1000], and the 99% confidence interval of $cov_s^{cs}(i, j)$ is calculated using the t-distribution.

In Figure 4A, the short covariances $cov_s(i, j)$ for $0 \le t \le 100$, $1000 \le t \le 1100$, $2000 \le t \le 2100$, and $3000 \le t \le 3100$ are shown as color matrices. When $cov_s(i, j)$ is inside the 99% confidence interval of $cov_s^{cs}(i, j)$, the value of $cov_s(i, j)$ is replaced by 0. Therefore, only the significant values of

$cov_s(i, j)$ are colorized in Figure 4. When $cov_s(i, j)$ takes positive (red) or negative (blue) values, the excitatory ensembles in the ith and jth modules exhibit in-phase and antiphase synchronization, respectively. We refer to this as intermodule synchronization. Moreover, it was also observed that the synchronized pairs were rearranged when a different short period was observed. We refer to such chaotic rearrangement of synchronized pairs as transitive chaotic synchronization.

Note that transitive chaotic synchronization is different from well-known transient chaos. Transient chaos is a phenomenon in which the system stays for a prolonged duration around a nonattracting chaotic set and then converges to another attractor, such as an equilibrium point or a periodic solution (Ott, 2002; Lai & Tel, 2011). Transient chaos is observed when the value of a parameter of the system is close to the bifurcation point at which the chaos becomes unstable. Similarly, transitive chaotic synchronization which we define here for the first time, is different from topological transitivity, which is an essential property of deterministic chaos with a strange attractor (Robinson, 1995; Kolyada & Snoha, 2009). Because transitive chaotic synchronization is also chaotic with positive Lyapunov exponents, it is topologically transitive. We define transitive chaotic synchronization as maintaining the rearrangements of synchronized pairs nonperiodically. Furthermore, the transitive chaotic synchronization considered here is similar to the Milnor attractor (Milnor, 1985), in which the system returns to a chaotic set with synchronized pairs after it successively moves away from it, due to the characteristics of both attracting and repelling orbits in this chaotic set. In other words, transitive chaotic synchronization maintains successive transitions among chaotic sets and may be related to chaotic itinerancy (Kanneko & Tsuda, 2001).

In the following, we examine how variation in s_I affects transitive chaotic synchronization.

The dynamics of the network for $s_I = -0.050$ are shown in Figure 3D, where the activity of excitatory neurons is dominant because of the small s_I. The short covariances $cov_s(i, j)$ for this dynamics are shown in Figure 4B. It was observed that the number of synchronized modules increases, but that transitive chaotic synchronization (chaotic rearrangement of synchronized pairs) still exists in this case.

The dynamics of the network for $s_I = -0.005$ are shown in Figure 3E, where the activity of inhibitory neurons is dominant because of the larger s_I. The short covariances $cov_s(i, j)$ for this dynamics are shown in Figure 4C. Here, the transitive chaotic synchronization disappeared, and oscillating modules were fixed. Note that the horizontal range in Figure 3E is narrower than that in Figure 3D to clearly show each oscillation. As demonstrated later, the nontransitive oscillations in Figure 3E were also chaotic, which we refer to as conventional chaos.

The dynamics of the network for $s_I = -0.005$ with a different initial condition (see appendix E) is shown in Figure 3F. It is observed that the

arrangement of oscillating modules in Figure 3F is different from that in Figure 3E. In the region of conventional chaos, at least several arrangements of oscillating modules coexist and the transitions among them are not observed. Although we can find other arrangements by using different initial conditions, we will not examine such arrangements further in this study because we are interested in the properties of transitive chaotic synchronization.

4 Analysis with Lyapunov Spectrum

To definitively state that the dynamics in Figure 3 are chaotic, we must show that the network has at least one positive Lyapunov exponent, which means that there is at least one direction in which two trajectories separate exponentially from each other.

In general, the number of Lyapunov exponents is n for an n-dimensional dynamical system, and a set of Lyapunov exponents is called the Lyapunov spectrum. In this study, we analyzed our network using the Fokker-Planck equations, which are a set of partial differential equations of phase θ and time t. Therefore, there is theoretically an infinite number of Lyapunov exponents in our model. When integrating the Fokker-Planck equations numerically, we transformed them into a set of ordinary differential equations using Fourier expansion as shown in appendix C. The Lyapunov spectrum can then be calculated by integrating these ordinary differential equations (Shimada & Nagashima, 1979; Nagashima & Baba, 1999).

It is known that there is always one Lyapunov exponent with a value of 0 for a continuous-time dynamical system, which we denoted as λ_0. Then we aligned the remaining Lyapunov exponents in descending order and denoted them as $\lambda_1, \lambda_2, \lambda_3, \ldots$. The dependence of the Lyapunov exponents $\lambda_0, \lambda_1, \lambda_6, \lambda_{11}, \lambda_{16}, \lambda_{21}$, and λ_{26} on s_I is shown in Figure 5A. The point and the error bar denote the mean and the 99% confidence interval calculated using the t-distribution for 10 trials, respectively. Methods for initializing 10 trials are explained in appendix E. We calculated at most 70 Lyapunov exponents depending on s_I and confirmed the sum of the calculated Lyapunov exponents at each s_I is negative, concluding this system is a dissipative one.

We found that positive Lyapunov exponents existed for all s_I values. Therefore, chaotic dynamics robustly exist over a wide range of s_I values in our model. This fact is related to the chaotic dynamics with balanced inhibition proposed by van Vreeswijk and Sompolinsky (1996).

In the region of transitive chaotic synchronization, the error bars for Lyapunov exponents are very narrow in Figure 5A so that they are not visible in this scale. This property would relate to the ergodic theorem that guarantees that the Lyapunov exponents take the same values for almost all the initial conditions on an attractor (Oseledets, 1968; Eckmann & Ruelle, 1985). On the other hand, in the region of conventional chaos, the error bars are
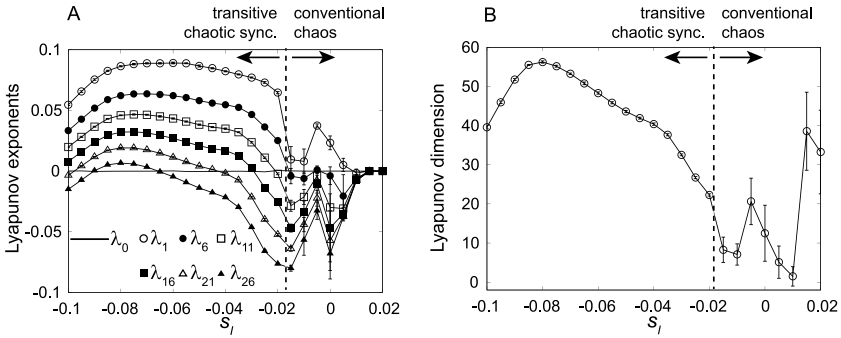
Figure 5: (A) The dependence of some Lyapunov exponents on s_I. This graph shows that there are some positive Lyapunov exponents for all s_I in this range. (B) The dependence of Lyapunov dimension on s_I.

wide because the Lyapunov exponents for different attractors are calculated as shown in Figures 3E and 3F.

We also calculated the Lyapunov dimension, or the Kaplan-York dimension (Kaplan & Yorke, 1979; Ott, 2002), defined as

$$D_L = K + \frac{1}{|\hat{\lambda}_{K+1}|} \sum_{j=1}^{K} \hat{\lambda}_j, \tag{4.1}$$

where K is the largest integer such that

$$\sum_{j=1}^{K} \hat{\lambda}_j \geq 0, \tag{4.2}$$

and $\hat{\lambda}_j (j \geq 1)$ is obtained by aligning $\lambda_i (i \geq 0)$ in descending order. The Lyapunov dimension is a type of fractal dimension that measures the geometrical object filled by an attractor in the phase space, as shown in Figure 5B. The point and the error bar denote the mean and the 99% confidence interval calculated using the t-distribution for 10 trials, respectively. The Lyapunov dimension became approximately 60 for $s_I = -0.08$. The chaotic oscillations in the 48 modules shown in Figure 3 correlated with each other because they were generated by intermodule connections. If such correlations become small and each oscillation is almost independent of the others, the Lyapunov dimension becomes large. Therefore, the modules for $s_I \simeq -0.08$ would show relatively independent chaotic oscillations compared to those for other values of s_I.

When s_I was increased toward -0.017, it was observed that D_L monotonically decreased, and when $s_I > -0.017$, the dependence of D_L on s_I became
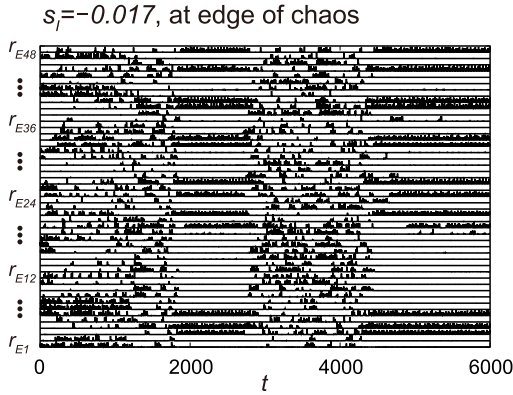
Figure 6: Intermittent switching between transitive chaotic synchronization and conventional chaos for $s_I = -0.017$, which would be related to the edge of chaos.

complicated. These results imply that transitive chaotic synchronization for $s_I < -0.017$ and conventional chaos for $s_I > -0.017$ were qualitatively different phenomena. As stated above, for $s_I > -0.017$, several arrangements of the oscillating modules can coexist. In this region, the Lyapunov dimension depends on the number of largely oscillating modules (e.g., 13 modules in Figure 3E and 12 modules in Figure 3F). Therefore, in the region of conventional chaos, the Lyapunov dimensions take different values for 10 trials.

Moreover, a transition from high ($\simeq 22$) dimensional chaos to low ($\simeq 8$) dimensional chaos took place at $s_I \simeq -0.017$. Around this transition point, we observed intermittent switching between transitive chaotic synchronization and conventional chaos, as shown in Figure 6.

Such intermittent switching is often observed at the edge of chaos. The "edge of chaos" refers to the area between order and disorder in the field of cellular automata and is also used in the field of dynamical systems (Pierre & Hübler, 1994; Melby et al., 2000). The edge of chaos in dynamical systems is typically observed when the largest positive Lyapunov exponent of the system approaches zero. In this case, intermittent switching between chaotic and nonchaotic dynamics was observed. However, in our model, intermittent switching between high-dimensional chaotic dynamics and low-dimensional chaotic dynamics was observed, as shown in Figure 6. Therefore, it is more appropriate to use the term "edge of high-dimensional chaos" in our system rather than "edge of chaos," but we will use the latter simpler term below to indicate this meaning.

To confirm the robustness of the observed phenomena, we regulated the strength of the connections instead of s_I. First, the strengths of the connections from the inhibitory neurons g_{EI} and g_{II} are replaced by $\gamma_{\text{from}I} g_{EI}$ and

$\gamma_{\text{from}I}g_{II}$, respectively, and $\gamma_{\text{from}I}$ is regulated. Similarly, the connections from excitatory neurons to inhibitory neurons, g_{IE} and h_{IE}, are replaced by $\gamma_{\text{to}I}g_{IE}$ and $\gamma_{\text{to}I}h_{IE}$, respectively. g_{EI}, g_{II}, and g_{IE} are the strengths of intramodule connections, and h_{IE} is the strength of intermodule connections, as shown in appendixes A and D. $\gamma_{\text{from}I}$ is related to the maturation of inhibitory neurons, and $\gamma_{\text{to}I}$ is related to the regulation of inhibitory neurons by excitatory neurons. The dependence of some Lyapunov exponents and Lyapunov dimensions on $\gamma_{\text{from}I}$ and $\gamma_{\text{to}I}$ is shown in Figure 7. The values of the parameters for $\gamma_{\text{from}I} = \gamma_{\text{to}I} = 1$ were the same as those used in Figure 3A. The point and the error bar denote the mean and the 99% confidence interval calculated using the t-distribution for 10 trials, respectively. Methods for initializing 10 trials are explained in appendix E. Similar to Figure 5, the largest positive Lyapunov exponents and Lyapunov dimensions become small when regulating $\gamma_{\text{from}I}$ or $\gamma_{\text{to}I}$, that is, a transition between transitive chaotic synchronization and conventional chaos occurs. Therefore, we regarded this transition as a robust phenomenon. Note that the Lyapunov dimension of the conventional chaos for $\gamma_{\text{from}I} = 0.8$ is larger than 10 because the number of largely oscillating modules tend to become large in this setting, as shown in Figure 7E, where 19 modules are oscillating.

Transitive chaotic synchronization is stable for large $\gamma_{\text{from}I}$ and small $\gamma_{\text{to}I}$. It is somewhat difficult to understand the opposite dependence of dynamics on the parameters, because the dynamics in our network is generated by reciprocal excitatory and inhibitory connections. However, the regulation of s_I yields clear results because it directly modulates the firing rates of inhibitory neurons. Therefore, as described in the following sections, we subsequently used s_I to regulate the E-I balance.

5 Measuring E-I Balance

In the previous sections, we identified several dynamics in our model by regulating the degree of inhibitory activity, s_I. With particular values of s_I, an optimal E-I balance in the network can be realized.

To measure the degree of E-I balance, we use two E/I ratios: the functional E/I ratio (fE/I) proposed by Bruining et al. (2020) and the input E/I ratio (iE/I), which is the proportion of excitatory to inhibitory input onto pyramidal neurons.

fE/I relates to detrended fluctuation analysis (DFA) (Peng et al., 1995; Linkenkaer-Hansen et al., 2001; Hardstone et al., 2012) to analyze the long-term correlations and scale-free properties of time series obtained from neural systems. In DFA, a time series is divided into bins with width w, and the trend in each bin is removed. Then the average $\langle F(w) \rangle$ over bins of standard deviation $F(w)$ of the detrended data in each window is calculated. When scaling $\langle F(w) \rangle \sim w^{\alpha}$ is observed, α is called the DFA exponent. Typical values of the DFA exponent are 0.5 for white noise, 1 for $1/f$ fluctuations, and
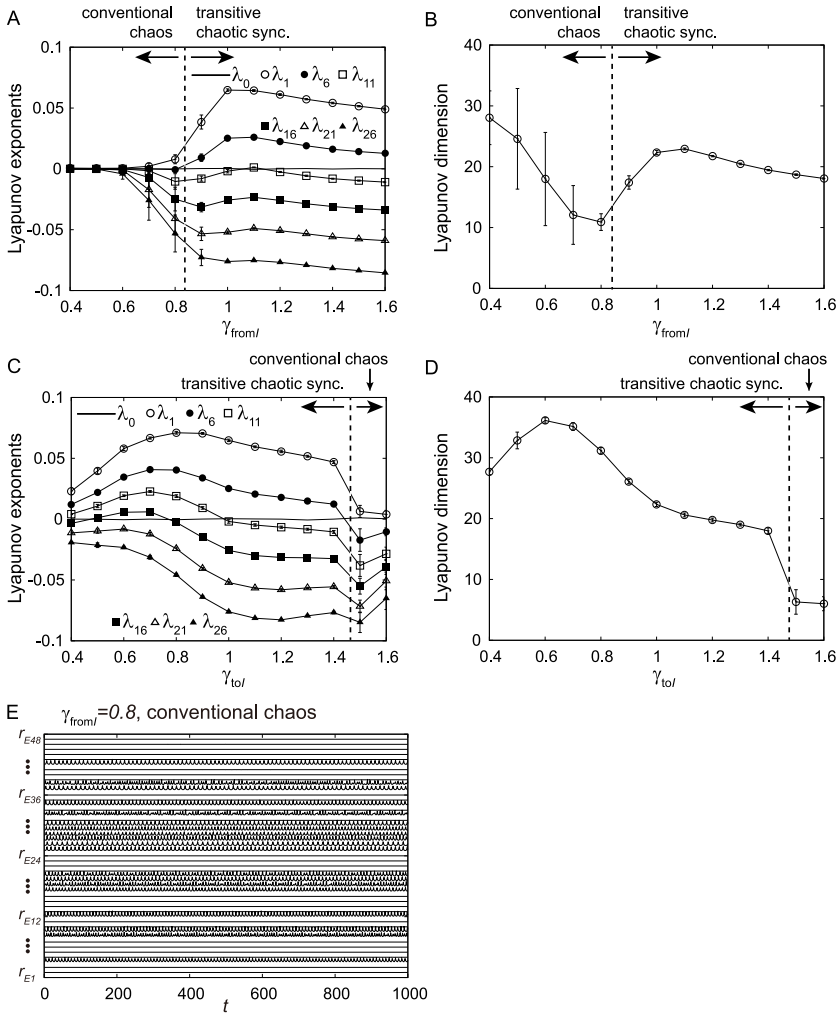
Figure 7: The dependence of (A, C) some Lyapunov exponents and (B, D) Lyapunov dimensions on the strengths of connections. The strengths of connections (A, B) from inhibitory neurons ($\gamma_{\text{from}I}g_{EI}$ and $\gamma_{\text{from}I}g_{II}$) or (C, D) from excitatory to inhibitory neurons ($\gamma_{\text{to}I}g_{IE}$ and $\gamma_{\text{to}I}h_{IE}$) are regulated. The values of the parameters for $\gamma_{\text{from}I} = \gamma_{\text{to}I} = 1$ are the same as those used in Figure 3A. (E) Temporal changes in the ensemble-averaged firing rates of excitatory neurons in a network with 48 modules for $\gamma_{\text{from}I} = 0.8$.

1.5 for Brownian motion. When the DFA exponent takes large values in the range (0.5, 1], the original time series has long-term correlations.

The DFA exponent carries some disadvantages when measuring the degree of E-I balance. First, a long time series is required to calculate the DFA exponent. Second, even when the DFA exponent can be obtained, the ratio of excitatory and inhibitory activity cannot be uniquely determined. The fE/I was then proposed to overcome these disadvantages (Bruining et al., 2020).

It takes a value of 1 when the DFA exponent reaches a maximum value by regulating the ratio of E-I activity. It is assumed that long-term correlation is maximal when optimal E-I balance is realized and that the maximal value of the DFA exponent is in the range (0.5, 1]. When the DFA exponent increases with an increase in excitatory activity, fE/I is defined as $fE/I < 1$. When the DFA exponent decreases with an increase in excitatory activity, fE/I is defined as $fE/I > 1$. The detailed method for calculating fE/I is presented in appendix F. When calculating it, the ensemble-averaged firing rate r_{Ei} for the ith module was used, and the average and standard deviation over the 48 modules were calculated.

For further comparison, we also calculated the simple input E/I ratio iE/I of the excitatory to inhibitory input onto pyramidal neurons, defined as

$$iE/I = \left\langle \frac{Input_{E \to Ei}}{Input_{I \to Ei}} \right\rangle_i , \tag{5.1}$$

$$Input_{E \to Ei} = \left\langle (g_{EE} - h_{EE})I_{Ei} + \sum_{j=1}^{M} h_{ij}^{EE} I_{Ej} \right\rangle_t , \tag{5.2}$$

$$Input_{I \to Ei} = \langle g_{EI} I_{Ii} \rangle_t , \tag{5.3}$$

where $Input_{E \to Ei}$ and $Input_{I \to Ei}$ are sums of excitatory and inhibitory synaptic inputs to the ith excitatory module and $\langle \cdot \rangle_t$ and $\langle \cdot \rangle_i$ denote an average over time t and an average over 48 modules, respectively. Note that they include both intra- and intermodule synaptic inputs. The meanings of the other parameters are explained in appendixes A, B, and D.

Although the definition of iE/I can be easily interpreted, it cannot be applied to experimental data in many cases. Conversely, fE/I can be calculated only from time series data obtained from neural systems because it quantifies long-term correlations and scale-free properties of data. For example, Bruining et al. (2020) applied fE/I to EEGs of healthy adults. We calculated both E/I ratios in our network for comparison. fE/I becomes important when we compare our theoretical results with experimental ones.

The dependence of fE/I and iE/I on s_I in our model is shown in Figure 8. The excitatory activity is dominant for small s_I because both fE/I and iE/I are larger than 1. The typical dynamics are shown in Figure 3D.
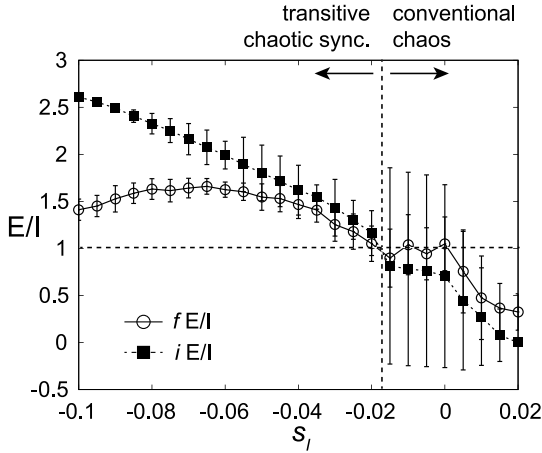
Figure 8: The dependence of fE/I and iE/I on s_I. Error bars denote the standard deviations over 48 modules.

It is observed that both fE/I and iE/I approach 1 when s_I is increased. $iE/I \simeq 1$ means that the network shows neither runaway excitation nor a quiescent state (Turrigiano & Nelson, 2004). However, the property of the dynamics with $iE/I \simeq 1$ is not clear when only iE/I is observed. In contrast, fE/I is calculated based on the analysis of the long-term correlations and scale-free properties of the data. Therefore, $fE/I \simeq 1$ means that the transitive chaotic synchronization shown in Figures 3A, 3B, and 3C has a long-term correlation.

For $s_I > -0.017$, both fE/I and iE/I become smaller than 1 (i.e., the inhibitory activity is dominant), and the conventional chaos in Figures 3E and 3F is observed.

In the following section, we show that transitive chaotic synchronization with fE/I, $iE/I \simeq 1$ is suitable for information processing.

6 Storing Randomly Varying Inputs via Reservoir Computing

Here, we demonstrate that transitive chaotic synchronization and the dynamics at the edge of chaos are suitable for information processing. Specifically, we consider the response of the network to time-varying inputs using the framework of reservoir computing (Lukoševičius & Jaeger, 2009) with respect to a short-term memory task. We demonstrate that a network showing transitive chaotic synchronization or dynamics at the edge of chaos displays a large memory capacity.

We define a time-varying input $u(t)$ as a binary signal whose value changes randomly every w_s,

$$u(t) = \begin{cases} +1 & \text{with probability } 0.5 \\ -1 & \text{otherwise} \end{cases}, \tag{6.1}$$

for $mw_s \leq t < (m+1)w_s$ ($m = 0, 1, 2, \ldots$). We set $w_s = 10$ so that the dynamics of the network can follow changes in $u(t)$.

We define the weights $g_i^{(in)}$ for the ith module as following a uniform distribution $[-I_s, I_s]$, where $I_s = 0.03$. $u(t)$ is assigned to the excitatory neurons in all modules by replacing the degree of excitatory activity s_{Ei} with $s_{Ei} + g_i^{(in)}u(t)$. Weights $g_i^{(in)}$ were fixed during the simulations.

In the following, we denote $u(t)$ for $mw_s \leq t < (m+1)w_s$ as u_m for discrete time steps $m = 0, 1, 2, \ldots$. Similarly, we obtain the output of the network for a discrete time step m as follows. First, the ensemble-averaged firing rate $r_{Ei}(t)$ of the excitatory ensemble in the ith module is binarized as follows:

$$\theta_{Ei}(t) = \begin{cases} 1 & \text{if } r_{Ei}(t) > 0.01, \\ 0 & \text{otherwise.} \end{cases} \tag{6.2}$$

Then $\theta_{Ei}(t)$ is averaged in the range $mw_s \leq t < (m+1)w_s$, and we denote it as $\hat{r}_{Eim}$ as follows:

$$\hat{r}_{Eim} = \frac{1}{w_s} \int_{mw_s}^{(m+1)w_s} \theta_{Ei}(t)\, dt. \tag{6.3}$$

Finally, the output o_m of the network for time step m is defined as a linear combination of 48 modules with a bias of

$$o_m = g_0 + \sum_{i=1}^{48} g_i\, \hat{r}_{Eim}. \tag{6.4}$$

Then the data for $0 \leq m < 1000$ were discarded, the data for $1000 \leq m < 2000$ were used to train g_i ($0 \leq i \leq 48$), and the data for $2000 \leq m < 3000$ were used as test data. We used the previous values of input u_{m-k} ($k = 1, 2, 3, \ldots$) for the target of o_m.

The weights g_i were trained to maximize the coefficient of determination between o_m and u_{m-k} for $1000 \leq m < 2000$. The maximum of the coefficient of determination is denoted as MF_k as follows:

$$MF_k = \max_{g_i} \frac{\text{cov}^2(o_m, u_{m-k})}{\sigma^2(o_m)\sigma^2(u_{m-k})}, \tag{6.5}$$
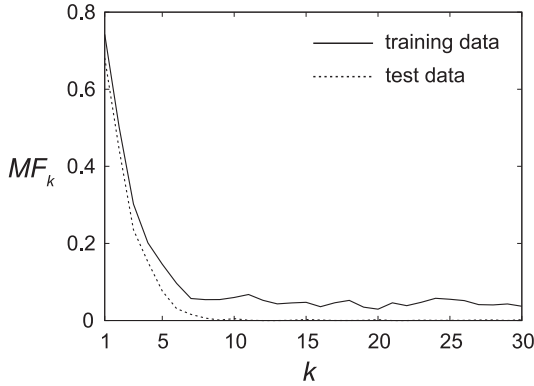
Figure 9: The dependence of MF_k on the time delay k for $s_I = -0.020$, where transitive chaotic synchronization is observed.

where $\sigma^2(o_m)$ and $\sigma^2(u_{m-k})$ are the variances of o_m and u_{m-k}, respectively, and $\mathrm{cov}(o_m, u_{m-k})$ is the covariance between o_m and u_{m-k}.

The dependence of MF_k on the time delay k for $s_I = -0.020$ where transitive chaotic synchronization is observed is shown in Figure 9. MF_k for the test data is also shown, which was obtained by calculating the coefficient of determination with the test data using g_i obtained from the training data. Whereas MF_k for the training data always takes positive values, MF_k for the test data takes positive values only when $k \leq 10$.

Using MF_k, the memory capacity MC is defined as the sum of MF_k over k as

$$MC = \sum_{k=1}^{k_{\max}} MF_k, \tag{6.6}$$

where $k_{\max} = 50$ in this study.

The dependence of MC on s_I for the training data ($1000 \leq m < 2000$) and the test data ($2000 \leq m < 3000$) is shown in Figure 10. We have shown MC before training for comparison, where the values of weights g_i are set following a uniform distribution $[-1, 1]$. All results were obtained by averaging 10 experiments for different $u(t)$.

Figure 10 shows that MC increases when s_I is close to -0.017 where transitive chaotic synchronization or dynamics at the edge of chaos are observed. For such values of s_I, both fE/I and iE/I are close to 1; therefore, it can be concluded that MC increases when an optimal E-I balance is realized. Although MC for test data was relatively small, it was larger than that before training. To obtain larger MC, all connections inside the network should be trained. Such training of the entire network is important for future comparison to the actual brain.
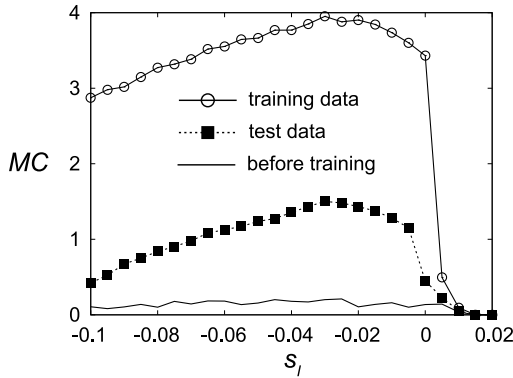
Figure 10: The dependence of *MC* on s_I. *MC*s for the training data ($1000 \le m < 2000$) and the test data ($2000 \le m < 3000$) are shown. *MC* before training is also shown for comparison. *MC* increases when s_I is close to -0.017, where transitive chaotic synchronization or dynamics at the edge of high-dimensional chaos is observed.

7 Conclusions and Discussion

In the field of nonlinear dynamics, it is well known that network models with balanced excitation and inhibition yield deterministic chaos (van Vreeswijk & Sompolinsky, 1996). The novelty of our study lies in the analysis of the Lyapunov spectrum and Lyapunov dimension, and the finding of more detailed properties of the chaotic dynamics with E-I balance (van Vreeswijk & Sompolinsky, 1996), namely, transitive chaotic synchronization, conventional chaos, and their intermittent switching at the edge of high-dimensional chaos with respect to the CP.

To understand the role of optimal E-I balance during the CP, we examined the dynamics of a network composed of excitatory pyramidal neurons (PYRs) in layers 2/3 and inhibitory interneurons (INs) in layer 4. INs with nicotinic acetylcholine receptors (nAChRs) in layer 1 were further connected to INs in layer 4. The effect of ACh was incorporated into the regulation of a parameter s_I of INs in layer 4.

In a randomly connected network of 48 such modules, transitive chaotic synchronization was observed in which modules that showed intermodule synchronization were rearranged transitively. When the activity of inhibitory neurons was dominant for a large s_I, conventional chaos was observed, in which modules that showed intramodule synchronization were fixed.

The parameter s_I can be interpreted as a constant input to inhibitory neurons, and we used it to regulate the E-I balance. Other methods for regulating E-I balance are available, such as regulating the ratio between the

numbers of excitatory and inhibitory neurons and regulating the strength of excitatory and inhibitory synapses. The former method cannot be applied to our model because the interactions among neurons are scaled as $1/N_X$ ($X = E$ or I), as shown in equation A.3. The latter method can be realized by regulating the strengths of the connections $g_{EE}, g_{IE}, g_{EI}, g_{II}, h_{EE}$, and h_{IE}. In Figure 7, the transition between transitive chaotic synchronization and conventional chaos was also observed when the strengths of connections from inhibitory neurons (g_{EI} and g_{II}) or from excitatory to inhibitory neurons (g_{IE} and h_{IE}) were regulated. Therefore, we regarded this transition as a robust phenomenon.

The Lyapunov dimension of transitive chaotic synchronization was high and that of conventional chaos was low. Around the boundary between these two regions, intermittent switching between transitive chaotic synchronization and conventional chaos was observed. Typical dynamics at the edge of chaos are intermittent switching between chaotic and nonchaotic dynamics (Pierre & Hübler, 1994; Melby et al., 2000). However, in our model, intermittent switching between high- and low-dimensional chaotic dynamics was observed. Therefore, a more suitable term than "edge of chaos" would be "edge of high-dimensional chaos."

To further investigate the relationship between E-I balance and chaotic dynamics in our network, we calculated two E/I ratios: the functional E/I ratio fE/I proposed by Bruining et al. (2020) and the input E/I ratio (iE/I) onto pyramidal neurons. Transitive chaotic synchronization and dynamics at the edge of high-dimensional chaos were observed when $fE/I, iE/I \simeq 1$. While $iE/I \simeq 1$ indicates neither runaway excitation nor a quiescent network state (Turrigiano & Nelson, 2004), the dynamics is not clear when only this ratio is taken. In contrast, fE/I is calculated based on the analysis of long-term correlations and scale-free properties of the data. Thus, it can be concluded that transitive chaotic synchronization and the dynamics at the edge of high-dimensional chaos with $fE/I \simeq 1$ show long-term correlations.

Finally, to examine the efficiency of information processing, a framework of reservoir computing (Lukoševičius & Jaeger, 2009) was introduced. A short-term memory task was performed by the network in which a time-varying random input was given, and the previous values of the input were obtained as the output of the network. It was found that memory capacity takes large values when transitive chaotic synchronization or dynamics at the edge of high-dimensional chaos were observed, where both fE/I and iE/I are close to 1. Therefore, it can be concluded that a network with optimal E-I balance offers large memory capacity. This result is similar to those of previous studies in which dynamics at the edge of chaos showed high performance in some tasks of the reservoir computing (Bertschinger & Natschläger, 2004; Legenstein & Maass, 2007; Boedecker et al., 2012). While previous studies have analyzed the dynamics at the edge of low-dimensional chaos, our network shows high-dimensional chaos with large

Lyapunov dimensions, realized by the network's multiple-module structure. The edge of high-dimensional chaos is a novel phenomenon that exists between transitive and conventional chaos. The dimension of chaos is expected to increase when the number of modules increases. Such high-dimensional chaos may be effective for certain tasks in reservoir computing. Uncovering such tasks will be investigated in future studies.

In the brain, the maturation of perisomatic GABA circuits achieves the optimal E-I balance that opens the CP (Hensch, 2005; Reh et al., 2020). Our finding that a network with E-I balance holds a large memory capacity indirectly supports the heightened learning capacity during these windows of brain development. When training a network under the reservoir computing framework, all connections in the network were fixed except those to the output neuron. To more accurately model learning during the CP, all connections inside the network should be trained. A procedure called force learning has been proposed to train recurrent neural networks, which successfully generates complex time-varying output patterns (Sussillo & Abbott, 2009). Such training of the entire network is important for future comparison to the actual brain.

Notably, CP timing is staggered across brain regions as each modality sequentially attains E-I balance (Reh et al., 2020). Mistimed or misaligned CP milestones may then amplify the progression toward cognitive disorders. In the literature on reservoir computing, various tasks, such as classification, parity check, and systems modeling, have been used as benchmarks (Bertschinger & Natschläger, 2004; Legenstein & Maass, 2007; Lukoševičius & Jaeger, 2009; Boedecker et al., 2012). As shown by Cramer et al. (2020) and Shi et al. (2022), the importance of "criticality" might depend on the complexity of the tasks. Similarly, the importance of the dynamics of the E-I balance might also depend on the properties of the tasks involving multiple brain areas. Analyses of such task dependence are planned for our future work.

Appendix A: Definition of a Single Module

In this appendix, we provide a detailed definition of the module model. A module of a network composed of N_E pyramidal neurons and N_I interneurons is defined using the following equations:

$$\tau_E \dot{\theta}_E^{(i)} = (1 - \cos\theta_E^{(i)}) + (1 + \cos\theta_E^{(i)})$$
$$\times (s_E + \xi_E^{(i)}(t) + g_{EE}I_E(t) - g_{EI}I_I(t)), \quad (A.1)$$

$$\tau_I \dot{\theta}_I^{(i)} = (1 - \cos\theta_I^{(i)}) + (1 + \cos\theta_I^{(i)})$$
$$\times (s_I + \xi_I^{(i)}(t) + g_{IE}I_E(t) - g_{II}I_I(t) + g_{gap}I_{gap}^{(i)}(t)), \quad (A.2)$$

$$I_X(t) = \frac{1}{2N_X} \sum_{j=1}^{N_X} \sum_k \frac{1}{\kappa_X} \exp\left(-\frac{t - t_k^{(j)}}{\kappa_X}\right), \tag{A.3}$$

$$I_{gap}^{(i)}(t) = \frac{1}{N_I} \sum_{j=1}^{N_I} \sin\left(\theta_I^{(j)}(t) - \theta_I^{(i)}(t)\right), \tag{A.4}$$

$$\langle \xi_X^{(i)}(t)\xi_Y^{(j)}(t')\rangle = D\delta_{XY}\delta_{ij}\delta(t - t'). \tag{A.5}$$

The internal states of the ith pyramidal neurons and ith interneurons are described by the phase variables $\theta_E^{(i)}$ and $\theta_I^{(i)}$, respectively (Kanamaru & Sekine, 2005). The activity of a single neuron in the model can be regulated by s_X ($X = E$ or I) when all connections are omitted, that is, $g_{EE} = g_{EI} = g_{IE} = g_{II} = g_{gap} = 0$. When $s_X < 0$, a stable equilibrium point $\theta = \theta_0 \equiv \arccos((1 + s_X)/(1 - s_X))$ exists and can be considered a resting state. When $s_X > 0$, the resting state disappears and θ starts to oscillate. Firing time is defined as the time at which $\theta_X^{(j)}$ exceeds π. In this study, we set $s_E, s_I < 0$. Each neuron without connections spontaneously fires owing to gaussian white noise $\xi_X^{(i)}(t)$ with strength D.

The connections among the neurons are global. We consider four types of intramodule connections: $E \to E$, $E \to I$, $I \to E$, and $I \to I$. Connections generating postsynaptic currents of an exponential form between all pairs of neurons, as well as diffusive connections between inhibitory neurons, are present. These two types of connections model chemical and electrical synapses with gap junctions, respectively. The form of the connections of the gap junctions is sinusoidal, following the Kuramoto model (Kuramoto, 1984) because our network is described by phase variables. $t_k^{(j)}$ is the kth firing time of the jth neuron. $g_{EE}, g_{IE}, -g_{EI}$, and $-g_{II}$ are connection weights within the excitatory and inhibitory ensembles, respectively, and g_{gap} is the strength of the gap junctions. τ_E and τ_I are the membrane time constants, and κ_E and κ_I are the time constants of the synaptic currents.

We set the values of the parameters as $s_E = -0.019$, $D = 0.0025$, $g_{EE} = 6$, $g_{IE} = g_{EI} = 2.8$, $g_{II} = 1$, $g_{gap} = 0.1$, $\tau_E = 1$, $\tau_I = 0.5$, $\kappa_E = 1$, and $\kappa_I = 1$.

Appendix B: The Fokker-Planck Equations

The averaged dynamics of a single module in the limit of $N_E, N_I \to \infty$ can be analyzed using the Fokker-Planck equations (FPEs) (Kuramoto, 1984; Kanamaru & Sekine, 2005), defined as follows:

$$\frac{\partial n_E}{\partial t} = -\frac{\partial}{\partial \theta_E}(A_E n_E) + \frac{D}{2}\frac{\partial}{\partial \theta_E}\left\{B_E \frac{\partial}{\partial \theta_E}(B_E n_E)\right\}, \tag{B.1}$$

$$\frac{\partial n_I}{\partial t} = -\frac{\partial}{\partial \theta_I}(A_I n_I) + \frac{D}{2}\frac{\partial}{\partial \theta_I}\left\{B_I \frac{\partial}{\partial \theta_I}(B_I n_I)\right\}, \tag{B.2}$$

$$A_E(\theta_E, t) = \frac{1}{\tau_E}(1 - \cos\theta_E) + \frac{1}{\tau_E}(1 + \cos\theta_E)$$
$$\times (s_E + g_{EE}I_E(t) - g_{EI}I_I(t)), \tag{B.3}$$

$$A_I(\theta_I, t) = \frac{1}{\tau_I}(1 - \cos\theta_I) + \frac{1}{\tau_I}(1 + \cos\theta_I)$$
$$\times (s_I + g_{IE}I_E(t) - g_{II}I_I(t) + g_{gap}I_{gap}(\theta_I, t)), \tag{B.4}$$

$$B_E(\theta_E, t) = \frac{1}{\tau_E}(1 + \cos\theta_E), \tag{B.5}$$

$$B_I(\theta_I, t) = \frac{1}{\tau_I}(1 + \cos\theta_I), \tag{B.6}$$

$$I_{gap}(\theta_I, t) = \langle\sin\theta_I\rangle\cos\theta_I - \langle\cos\theta_I\rangle\sin\theta_I, \tag{B.7}$$

$$\langle f(\theta_I)\rangle = \int_0^{2\pi} f(\theta_I)\, n_I(\theta_I, t)\, d\theta_I, \tag{B.8}$$

for the normalized number densities $n_E(\theta_E, t)$ and $n_I(\theta_I, t)$ of the excitatory and inhibitory neurons, respectively. In the limit of $N_E, N_I \to \infty$, $n_E(\theta_E, t)$ and $n_I(\theta_I, t)$ are defined as follows:

$$n_E(\theta_E, t) \equiv \frac{1}{N_E}\sum \delta(\theta_E^{(i)} - \theta_E), \tag{B.9}$$

$$n_I(\theta_I, t) \equiv \frac{1}{N_I}\sum \delta(\theta_I^{(i)} - \theta_I). \tag{B.10}$$

The probability fluxes for excitatory neurons and inhibitory neurons are defined as

$$r_E(\theta_E, t) = A_E n_E - \frac{D}{2}B_E\frac{\partial}{\partial\theta_E}(B_E n_E), \tag{B.11}$$

$$r_I(\theta_I, t) = A_I n_I - \frac{D}{2}B_I\frac{\partial}{\partial\theta_I}(B_I n_I). \tag{B.12}$$

$r_E \equiv r_E(\pi, t)$ and $r_I \equiv r_I(\pi, t)$ can be interpreted as ensemble-averaged firing rates for excitatory and inhibitory neurons.

Using r_E and r_I, the excitatory current $I_E(t)$ and the inhibitory current $I_I(t)$ in the intramodule connections are governed by the following equations:

$$\dot{I_X}(t) = -\frac{1}{\kappa_X}\left(I_X(t) - \frac{1}{2}r_X\right). \tag{B.13}$$

Using FPEs, we can obtain the theoretical dynamics of ensemble-averaged firing rates r_E and r_I, and various methods for nonlinear analysis can be used.

In this study, we examined the network in the limit of $N_E, N_I \to \infty$ by analyzing FPEs B.1 and B.2, which describe the dynamics of globally connected E-I neurons governed by equations A.1 and A.2. The dynamics of randomly connected E-I neurons with probability p is also described by FPEs B.1 and B.2. In such a network, N_X in the denominator and the summation over j in equation A.3 are replaced by pN_X and summation over a set of pN_X neurons, respectively. This equivalence between a global network and a random network is caused by the scaling factor $1/N_X$ in equation A.3 and the large N_X limit. The infinitesimally small connections of order $1/N_X$ differ from the strong connections of order $1/\sqrt{N_X}$ in previous studies (Renart et al., 2010; van Vreeswijk & Sompolinsky, 1996). Despite the different orders of connections, the E-I balance is important in all networks.

Appendix C: Numerical Integration of the Fokker-Planck Equations

In this appendix, we describe a method for the numerical integration of FPEs B.1 and B.2 (Kanamaru & Sekine, 2005; Kanamaru & Aihara, 2008). Because the two densities n_E and n_I are 2π-periodic functions of θ_E and θ_I, respectively, they can be expanded as

$$n_E(\theta_E, t) = \frac{1}{2\pi} + \sum_{k=1}^{\infty} (a_k^E(t)\cos(k\theta_E) + b_k^E(t)\sin(k\theta_E)), \quad \text{(C.1)}$$

$$n_I(\theta_I, t) = \frac{1}{2\pi} + \sum_{k=1}^{\infty} (a_k^I(t)\cos(k\theta_I) + b_k^I(t)\sin(k\theta_I)), \quad \text{(C.2)}$$

and by substituting them, equations B.1 and B.2 are transformed into a set of ordinary differential equations of a_k^X and b_k^X as follows:

$$\frac{da_k^{(X)}}{dt} = -(s_X + \tilde{I}_X + 1)\frac{k}{\tau_X}b_k^{(X)} - (s_X + \tilde{I}_X - 1)\frac{k}{2\tau_X}(b_{k-1}^{(X)} + b_{k+1}^{(X)})$$

$$- \frac{Dk}{8\tau_X^2}f(a_k^{(X)}) + \frac{\pi g_{gap}k}{4\tau_X}(-b_1 g_1(b_k^{(X)}) + a_1 g_2(a_k^{(X)}))\delta_{XI}, \quad \text{(C.3)}$$

$$\frac{db_k^{(X)}}{dt} = (s_X + \tilde{I}_X + 1)\frac{k}{\tau_X}a_k^{(X)} + (s_X + \tilde{I}_X - 1)\frac{k}{2\tau_X}(a_{k-1}^{(X)} + a_{k+1}^{(X)})$$

$$- \frac{Dk}{8\tau_X^2}f(b_k^{(X)}) + \frac{\pi g_{gap}k}{4\tau_X}(b_1 g_1(a_k^{(X)}) + a_1 g_2(b_k^{(X)}))\delta_{XI}, \quad \text{(C.4)}$$

$$f(x_k) = (k-1)x_{k-2} + 2(2k-1)x_{k-1} + 6kx_k$$

$$+ 2(2k+1)x_{k+1} + (k+1)x_{k+2}, \tag{C.5}$$

$$g_1(x_k) = x_{k-2} + 2x_{k-1} + 2x_k + 2x_{k+1} + x_{k+2}, \tag{C.6}$$

$$g_2(x_k) = x_{k-2} + 2x_{k-1} - 2x_{k+1} - x_{k+2}, \tag{C.7}$$

$$\tilde{I}_X \equiv g_{XE}I_E - g_{XI}I_I, \tag{C.8}$$

$$a_0^{(X)} \equiv \frac{1}{\pi}, \tag{C.9}$$

$$b_0^{(X)} \equiv 0, \tag{C.10}$$

$$a_{-n}^{(X)} \equiv a_n^{(X)}, \tag{C.11}$$

$$b_{-n}^{(X)} \equiv -b_n^{(X)}, \tag{C.12}$$

where $X = E$ or I. Using a vector $x = (I_E, I_I, a_1^E, b_1^E, a_1^I, b_1^I, a_2^E, b_2^E, a_2^I, b_2^I, \ldots)^t$, the ordinary differential equations $\dot{x} = f(x)$ are defined by equations B.13, C.3, and C.4. By numerically integrating these ordinary differential equations, the time series of the ensemble-averaged firing rates r_E and r_I are obtained. For the numerical calculations, each Fourier series is truncated at the first 60 terms; therefore, x is approximated by a 242-dimensional vector.

Appendix D: Connections among Modules

To obtain a network of M modules, we defined the connection strengths T_{Ei} and T_{Ii} of the input to the excitatory and inhibitory neurons in the ith module as follows:

$$T_{Ei} = (g_{EE} - h_{EE})I_{Ei} - g_{EI}I_{Ii} + \sum_{j=1}^{M} h_{ij}^{EE} I_{Ej}, \tag{D.1}$$

$$T_{Ii} = (g_{IE} - h_{IE})I_{Ei} - g_{II}I_{Ii} + \sum_{j=1}^{M} h_{ij}^{IE} I_{Ej}, \tag{D.2}$$

where I_{Ei} and I_{Ii} are the sums of the postsynaptic currents of the ith module defined by equation A.3. We replaced the inputs to the excitatory and inhibitory neurons used in equations A.1 and A.2 with T_{Ei} and T_{Ii}.

In the definitions above, the intramodule connection weights g_{EE} and g_{IE} are decreased by subtracting h_{EE} and h_{IE}, respectively, to maintain the chaotic dynamics observed in a module.

The intermodule connection weights h_{ij}^{EE} and h_{ij}^{IE} are defined randomly as follows:

$$h_{ij}^{EE} = \begin{cases} \dfrac{1}{Mp} \, h_{EE}, & \text{with probability } p, \\ 0, & \text{otherwise.} \end{cases} \tag{D.3}$$

$$h_{ij}^{IE} = \begin{cases} \dfrac{1}{Mp} \, h_{IE}, & \text{with probability } p, \\ 0, & \text{otherwise.} \end{cases} \tag{D.4}$$

We set the values of the parameters as $M = 48$, $p = 0.1$, $h_{IE} = 1.2$, and $h_{EI} = 1.9$.

Appendix E: Initialization of Models

In this appendix, we explain methods for initializing our models.

In Figures 2A, 2B, 2D, and 2E, the dynamics of a module model composed of N_E excitatory neurons and N_I inhibitory neurons defined by equations A.1 and A.2 is shown. In this model, $\theta_E^{(i)}$ and $\theta_I^{(i)}$ were initialized to random values obtained from a uniform distribution in $[0, 2\pi]$. Discarding the transient data until $t = 1000$, the results in Figures 2A, 2B, 2D, and 2E were obtained.

In Figure 2C, a module model was analyzed by FPEs. As shown in appendix C, FPEs can be analyzed by ordinary differential equations B.13, C.3, and C.4 for a vector $x = (I_E, I_I, a_1^E, b_1^E, a_1^I, b_1^I, a_2^E, b_2^E, a_2^I, b_2^I, \ldots)^t$, which includes Fourier series of probability densities n_E and n_I. This vector x cannot be initialized randomly because it should satisfy the following conditions for probability density n_X ($X = E$ of I):

$$n_X(\theta_X, 0) \geq 0,$$

$$\int_0^{2\pi} n_X(\theta_X, 0) = 1.$$

Instead, we initialized x to 0, which corresponds to a uniform distribution

$$n_X(\theta_X, 0) = \frac{1}{2\pi},$$

as shown in equations C.1 and C.2. When the transient data until $t = 1000$ are discarded, the result in Figure 2C was obtained.

In Figure 3, the dynamics of a network with 48 modules is analyzed by FPEs. When all the vectors x of 48 modules are initialized to 0, the simulation starts from a fully synchronized state of 48 modules. To avoid such a fully synchronized initial condition, we prepared 48 different vectors x using the following method. First, we simulated a single module for s_I with an initial condition $x = 0$ until $t = t_1$, and we denote the obtained vector as $x_1(t_1; s_I)$.

Then we initialized the ith module of 48 modules to $x_1(t_1 + (i-1)dt_1; s_I)$ $(i = 1, 2, \ldots, 48)$, and we simulated the network with 48 modules until $t = t_2$. The obtained vector is denoted as $x_{48}(t_1, dt_1, t_2; s_I)$, and it can be used as an initial vector for the network with 48 modules. In Figures 3A, 3B, 3D, and 3E, $x_{48}(10,000, 0.01, 10,000; -0.013)$ was used for initialization. In Figures 3C and 3F, $x_{48}(10,000, 0.01, 10,000; -0.020)$ was used for initialization. When the transient data until $t = 4000$ were discarded, the results in Figure 3 were obtained.

In Figures 4 and 6, $x_{48}(10,000, 0.01, 10,000; -0.013)$ was used for initialization, and the transient data until $t = 4000$ were discarded.

When calculating N_L Lyapunov exponents as shown in Figures 5, 7A, 7B, 7C, and 7D, we have to compute $N_L + 1$ trajectories. We calculate them for 10 trials. We initialized the network to $x_{48}(10,000, 0.01, 10,000 + 0.1(i-1); -0.013)$ $(i = 1, 2, \ldots N_L + 1)$ for the first trial, and we initialized them to $x_{48}(10,000, 0.01, 10,000 + 0.1(i-1); -0.020 - 0.001(j-2))$ $(i = 1, 2, \ldots N_L + 1)$ for the jth $(j = 2, 3, \ldots, 10)$ trial. Discarding transient data until $t = 4000$, Lyapunov exponents were calculated by using the dynamics until $t = 50,000$.

In Figure 7E, $x_{48}(10,000, 0.01, 10,000; -0.021)$ was used for initialization, and the transient data until $t = 4000$ were discarded.

In Figures 8, 9, and 10, $x_{48}(10,000, 0.01, 10,000; -0.013)$ was used for initialization, and the transient data until $t = 4000$ were discarded.

Appendix F: Calculation of fE/I

Here, we introduce a method for calculating fE/I (Bruining et al., 2020).

1. Typically, a bandpass filter is applied to the data. Bruining et al. (2020) applied a bandpass filter with a frequency range of 8 to 13 Hz to electroencephalogram data. However, in this study, a bandpass filter was not applied because our data were obtained from numerical simulations.

2. The envelope of the data is obtained by applying the Hilbert transform. We denote the obtained envelope as $A(t)$ $(t = 1, 2, 3, \ldots)$ and denote its average over time as $\langle A \rangle$.

3. The cumulative sum $S(t)$ of $A(t)$ is calculated as follows:

$$S(t) = \sum_{k=1}^{t} (A(k) - \langle A \rangle). \tag{F.1}$$

4. The time axis is divided into bins of width w, and $S_1(t) = S(t)/\langle A \rangle_w$ is calculated, where $\langle A \rangle_w$ is the average of $A(t)$ in each bin.

5. A linear fit $l_w(t)$ of $S_1(t)$ in each bin was calculated, and $S_2(t) = S_1(t) - l_w(t)$ was calculated.

6. The standard deviation nF of $S_2(t)$ in each bin is calculated.

7. The correlation coefficient C of $\langle A \rangle_w$ and nF is calculated. Subsequently, fE/I is defined as $fE/I = 1 - C$.

Acknowledgments

References

Bertschinger, N., & Natschläger, T. (2004). Real-time computation at the edge of chaos in recurrent neural networks. *Neural Computation*, *16*, 1413–1436. 10.1162/089976604323057443

Boedecker, J., Obst, O., Lizier, J. T., Mayer, N. M., & Asada, M. (2012). Information processing in echo state networks at the edge of chaos. *Theory in Biosciences*, *131*, 205–213. 10.1007/s12064-011-0146-8

Bruining, H., Hardstone, R., Juarez-Martinez, E. L., Sprengers, J., Avramiea, A.-E., Simpraga, S., . . . Linkenkaer-Hansen, K. (2020). Measurement of excitation-inhibition ratio in autism spectrum disorder using critical brain dynamics. *Scientific Reports*, *10*, 9195. 10.1038/s41598-020-65500-4

Brunel, N. (2000). Dynamics of sparsely connected networks of excitatory and inhibitory spiking neurons. *Journal of Computational Neuroscience*, *8*, 183–208. 10.1023/A:1008925309027

Cramer, B., Stöckel, D., Kreft, M., Wibral, M., Schemmel, J., Meiner, K., & Priesemann, V. (2020). Control of criticality and computation in spiking neuromorphic networks with plasticity. *Nature Communications*, *11*, 2853.

Eckmann, J. P., & Ruelle, D. (1985). Ergodic theory of chaos and strange attractors. *Reviews of Modern Physics*, *57*, 617–656. 10.1103/RevModPhys.57.617

Eichler, S. A., & Meier, J. C. (2008). E-I balance and human diseases—from molecules to networking. *Frontiers in Molecular Neuroscience*, *1*, 1–5. 10.3389/neuro.02.002.2008

Hardstone, R., Poil, S.-S., Schiavone, G., Jansen, R., Nikulin, V. V., Mansvelder, H. D., & Linkenkaer-Hansen, K. (2012). Detrended fluctuation analysis: A scale-free view on neuronal oscillations. *Frontiers in Physiology*, *3*, 450. 10.3389/fphys.2012.00450

Hensch, T. K. (2004). Critical period regulation. *Annual Review of Neuroscience*, *27*, 549–579. 10.1146/annurev.neuro.27.070203.144327

Hensch, T. K. (2005). Critical period plasticity in local cortical circuits. *Nature Reviews Neuroscience*, *6*, 877–888. 10.1038/nrn1787

Hodgkin, A. L. (1948). The local electric changes associated with repetitive action in a non-medullated axon. *Journal of Physiology*, *107*, 165–181. 10.1113/jphysiol.1948.sp004260

Hubel, D. H., & Wiesel, T. N. (1970). The period of susceptibility to the physiological effects of unilateral eye closure in kittens. *Journal of Physiology*, *206*, 419–436. 10.1113/jphysiol.1970.sp009022

Izhikevich, E. M. (1999). Class 1 neural excitability, conventional synapses, weakly connected networks, and mathematical foundations of pulse-coupled models. *IEEE Transactions on Neural Networks and Learning Systems*, *10*, 499–507. 10.1109/72.761707

Izhikevich, E. M. (2000). Neural excitability, spiking and bursting. *International Journal of Bifurcation and Chaos*, *10*, 1171–1266.

Kanamaru, T. (2006). Blowout bifurcation and on-off intermittency in pulse neural networks with multiple modules. *International Journal of Bifurcation and Chaos*, *16*, 3309–3321. 10.1142/S021812740601680X

Kanamaru, T. (2007). Chaotic pattern transitions in pulse neural networks. *Neural Networks*, *20*, 781–790. 10.1016/j.neunet.2007.06.002

Kanamaru, T., & Aihara, K. (2008). Stochastic synchrony of chaos in a pulse coupled neural network with both chemical and electrical synapses among inhibitory neurons. *Neural Computation*, *20*, 1951–1972. 10.1162/neco.2008.05-07-516

Kanamaru, T., & Aihara, K. (2019). Acetylcholine-mediated top-down attention improves the response to bottom-up inputs by deformation of the attractor landscape. *PLOS ONE*, *14*, e0223592. 10.1371/journal.pone.0223592

Kanamaru, T., Fujii, H., & Aihara, K. (2013). Deformation of attractor landscape via cholinergic presynaptic modulations: A computational study using a phase neuron model. *PLOS ONE*, *8*, e53854. 10.1371/journal.pone.0053854

Kanamaru, T., & Sekine, M. (2005). Synchronized firings in the networks of class 1 excitable neurons with excitatory and inhibitory connections and their dependences on the forms of interactions. *Neural Computation*, *17*, 1315–1338. 10.1162/0899766053630387

Kaneko, K., & Tsuda, I. (2001). *Complex systems: Chaos and beyond*. Springer.

Kaplan, J. L., & Yorke, J. A. (1979). Chaotic behavior of multidimensional difference equations. In H. O. Peitgen & H. O. Walther (Eds.), *Functional differential equations and approximations of fixed points*. Lecture Notes in Mathematics, vol. 730. Springer.

Kolyada, S., & Snoha, L. (2009). Topological transitivity. *Scholarpedia*, *4*, 5802.

Kubota, T., Nakajima, K., & Takahashi, H. (2018). Information processing using a single Izhikevich neuron. In *Proceedings of ALIFE 2018: The 2018 Conference on Artificial Life* (pp. 550–557).

Kuramoto, Y. (1984). *Chemical oscillations, waves, and turbulence*. Springer.

Lai, Y.-C., & Tel, T. (2011). *Transient chaos, complex dynamics on finite time scales*. Springer.

Legenstein, R., & Maass, W. (2007). Edge of chaos and prediction of computational performance for neural circuit models. *Neural Networks*, *20*, 323–334. 10.1016/j.neunet.2007.04.017

Linkenkaer-Hansen, K., Nikouline, V. V., Palva, J. M., & Ilmoniemi, R. J. (2001). Long-range temporal correlations and scaling behavior in human brain oscillations. *Journal of Neuroscience*, *15*, 1370–1377. 10.1523/JNEUROSCI.21-04-01370.2001

Lukoševičius, M., & Jaeger, H. (2009). Reservoir computing approaches to recurrent neural network training. *Computer Science Review*, *3*, 127–149.

Madsen, J., & Parra, L. C. (2022). Cognitive processing of a common stimulus synchronizes brains, hearts, and eyes. *PNAS Nexus*, *1*, pgac020. 10.1093/pnasnexus/pgac020

Melby, P., Kaidel, J., Weber, N., & Hübler, A. (2000). Adaptation to the edge of chaos in the self-adjusting logistic map. *Physical Review Letters*, *84*, 5991–5993. 10.1103/PhysRevLett.84.5991

Milnor, J. (1985). On the concept of attractor. *Communications in Mathematical Physics*, *99*, 177–195. 10.1007/BF01212280

Morishita, H., Miwa, J. M., Heintz, N., & Hensch, T. K. (2010). Lynx1, a cholinergic brake, limits plasticity in adult visual cortex. *Science*, *330*, 1238–1240. 10.1126/science.1195320

Nagashima, H., & Baba, Y. (1999). *Introduction to chaos*. Institute of Physics Publishing.

Nelson, S. B., & Valakh, V. (2015). Excitatory/inhibitory balance and circuit homeostasis in autism spectrum disorders. *Neuron*, *87*, 684–698. 10.1016/j.neuron.2015.07.033

Oseledets, V. I. (1968). A multiplicative ergodic theorem. Characteristic Ljapunov, exponents of dynamical systems. *Transactions of the Moscow Mathematical Society*, *19*, 197–231.

Ott, E. (2002). *Chaos in dynamical systems* (2nd ed.). Cambridge University Press.

Peng, C.-K., Havlin, S., Stanley, H. E., & Goldberger, A. L. (1995). Quantification of scaling exponents and crossover phenomena in nonstationary heartbeat time series. *Chaos*, *5*, 82–87. 10.1063/1.166141

Pierre, D., & Hübler, A. (1994). A theory for adaptation and competition applied to logistic map dynamics. *Physica D*, *7*, 343–360. 10.1016/0167-2789(94)90292-5

Reh, R. K., Dias, B. G., Nelson, C. A. III, Kaufer, D., Werker, J. F., Kolb, B., . . . Hensch, T. K. (2020). Critical period regulation across multiple timescales. In *Proceedings of the National Academy of Sciences USA*, *117*, 23242–23251. 10.1073/pnas.1820836117

Renart, A., Rocha, J., Bartho, P., Hollender, L., Parga, N., Reyes, A., & Harris, K. D. (2010). The asynchronous state in cortical circuits. *Science*, *327*, 587–590. 10.1126/science.1179850

Robinson, C. (1995). *Dynamical systems: Stability, symbolic dynamics, and chaos*. CRC Press.

Rodriguez, A., Whitson, J., & Granger, R. (2004). Derivation and analysis of basic computational operations of thalamocortical circuits. *Journal of Cognitive Neuroscience*, *16*, 856–877. 10.1162/089892904970690

Shi, J., Kirihara, K., Tada, M., Fujioka, M., Usui, K., Koshiyama, D., . . . Aihara, K. (2022). Criticality in the healthy brain. *Frontier in Network Physiology*, *1*, 755685.

Shimada, I., & Nagashima, H. (1979). A numerical approach to ergodic problem of dissipative dynamical systems. *Progress of Theoretical Physics*, *61*, 1605–1616. 10.1143/PTP.61.1605

Shu, Y., Hasenstaub, A., & McCormick, D. A. (2003). Turning on and off recurrent balance cortical activity. *Nature*, *423*, 288–293. 10.1038/nature01616

Sussillo, D., & Abbott, L. F. (2009). Generating coherent patterns of activity from chaotic neural networks. *Neuron*, *63*, 544–557. 10.1016/j.neuron.2009.07.018

Takesian, A. E., Bogart, L. J., Lichtman, J. W., & Hensch, T. K. (2018). Inhibitory cir-
    cuit gating of auditory critical period plasticity. *Nature Neuroscience*, *21*, 218–227.
    10.1038/s41593-017-0064-2

Tanaka, T., Nakajima, K., & Aoyagi, T. (2020). Effect of recurrent infomax on the in-
    formation processing capability of input-driven recurrent neural networks. *Neu-
    roscience Research*, *156*, 225–233. 10.1016/j.neures.2020.02.001

Thiele, A., & Bellgrove, M. A. (2018). Neuromodulation of attention. *Neuron*, *97*, 769–
    785. 10.1016/j.neuron.2018.01.008

Turrigiano, G. G., & Nelson, S. B. (2004). Homeostatic plasticity in the developing
    nervous system. *Nature Reviews Neuroscience*, *5*, 97–107. 10.1038/nrn1327

van Vreeswijk, C., & Sompolinsky, H. (1996). Chaos in neuronal networks with bal-
    anced excitatory and inhibitory activity. *Science*, *274*, 1724–1726. 10.1126/science
    .274.5293.1724

Werker, J. F., & Hensch, T. K. (2015). Critical periods in speech perception: new
    directions. *Annual Review of Psychology*, *66*, 173–196. 10.1146/annurev-psych
    -010814-015104

Yizhar, O., Fenno, L. E., Prigge, M., Schneider, F., Davidson, T. J., O'Shea, D. J.,
    . . . Deisseroth, K. (2011). Neocortical excitation/inhibition balance in information
    processing and social dysfunction. *Nature*, *477*, 171–178. 10.1038/nature10360